

Field-induced hybridization of moiré excitons in MoSe₂/WS₂ heterobilayers

Borislav Polovnikov,^{1,2,*} Johannes Scherzer,¹ Subhradeep Misra,¹ Xin Huang,^{1,3,4}
Christian Mohl,¹ Zhijie Li,¹ Jonas Göser,¹ Jonathan Förste,¹ Ismail Bilgin,¹ Kenji
Watanabe,⁵ Takashi Taniguchi,⁶ Alexander Högele,^{1,7,†} and Anvar S. Baimuratov^{1,‡}

¹*Fakultät für Physik, Munich Quantum Center, and Center for NanoScience (CeNS),
Ludwig-Maximilians-Universität München, Geschwister-Scholl-Platz 1, 80539 München, Germany*

²*Max-Planck-Institut für Quantenoptik, Hans-Kopfermann-Straße 1, 85748 Garching bei München, Germany*

³*Beijing National Laboratory for Condensed Matter Physics, Institute of Physics,
Chinese Academy of Sciences, Beijing 100190, People's Republic of China*

⁴*School of Physical Sciences, CAS Key Laboratory of Vacuum Physics,
University of Chinese Academy of Sciences, Beijing 100190, People's Republic of China*

⁵*Research Center for Functional Materials, National Institute for Materials Science, 1-1 Namiki, Tsukuba 305-0044, Japan*

⁶*International Center for Materials Nanoarchitectonics,
National Institute for Materials Science, 1-1 Namiki, Tsukuba 305-0044, Japan*

⁷*Munich Center for Quantum Science and Technology (MCQST), Schellingstraße 4, 80799 München, Germany*

(Dated: February 19, 2024)

We study experimentally and theoretically the hybridization among intralayer and interlayer moiré excitons in a MoSe₂/WS₂ heterostructure with antiparallel alignment. Using a dual-gate device and cryogenic white light reflectance and narrow-band laser modulation spectroscopy, we subject the moiré excitons in the MoSe₂/WS₂ heterostack to a perpendicular electric field, monitor the field-induced dispersion and hybridization of intralayer and interlayer moiré exciton states, and induce a cross-over from type I to type II band alignment. Moreover, we employ perpendicular magnetic fields to map out the dependence of the corresponding exciton Landé g -factors on the electric field. Finally, we develop an effective theoretical model combining resonant and non-resonant contributions to moiré potentials to explain the observed phenomenology, and highlight the relevance of interlayer coupling for structures with close energetic band alignment as in MoSe₂/WS₂.

©2024 American Physical Society

Two dimensional transition metal dichalcogenides (TMDs) [1–3] and vertically stacked van der Waals heterostructures [4] have emerged as increasingly significant materials for condensed matter research. Stacking two atomically thin layers with small lattice mismatch or rotational misalignment generally results in a new, long-range moiré superlattice that introduces a periodic potential for charge-carriers and provides a scaffold for ordered electronic states [5–7]. The periodicity of the moiré potential depends sensitively on the rotation angle between the layers [8], providing means to engineer the physical properties of van der Waals structures and to favor the formation of correlated many-body states [9].

In their monolayer limit TMDs host tightly bound excitons with large binding energy and strong light-matter interaction [1]. In twisted or lattice-incommensurate TMD heterobilayers, the presence of a moiré potential leads to the emergence of distinct moiré excitons that can be used to study electronic states optically [10, 11], including signatures of Hubbard model physics and correlation-induced magnetism [12, 13], Wigner crystallization of charge carriers [14, 15] or correlated Mott-insulator states [14, 16–21].

The MoSe₂/WS₂ heterostructure, which has previously been shown to host correlated electronic states [22, 23], deserves particular analysis. Unlike in WS₂/WSe₂ or MoSe₂/WSe₂, which have conduction (CB) and valence band (VB) offsets of a few hundreds of meV, first-

principle calculations have shown that the CBs of MoSe₂ and WS₂ are much closer [24]. However, their precise energetic ordering, and hence the nature of the lowest energy moiré excitons in MoSe₂/WS₂, remain matter of continuing debate, with reported CB offset values between -20 meV [25] and $+100$ meV [23]. Moreover, early studies mostly focused on a parallel (R-type) stacking configuration with opposite spins in the lowest conduction subbands. In this work, by using complementary experimental and theoretical techniques, we present a comprehensive study of antiparallel (H-type) MoSe₂/WS₂ that unveils an intricate interplay of both intra- and interlayer moiré excitons and allows to unambiguously determine the nature of the observed optical resonances.

To control the resonance energy of interlayer excitons we fabricated a dual-gate field-effect device with the schematics shown in Fig. 1a, consisting of a MoSe₂/WS₂ heterobilayer encapsulated by symmetric hexagonal boron nitride (hBN) spacers of 55 nm each with few-layer graphite electrodes (G) as the top and bottom gates. Applying opposite gate voltages V_B and $V_T = -V_B$ subjects the device to a perpendicular electric field proportional to $\Delta V_{TB} = V_B - V_T$. By using crystals synthesized with chemical vapor deposition [26], we controlled the orientation of the monolayers by optically aligning the edges of the flakes and fabricated a sample with a $179 \pm 1^\circ$ angle [27]. In this case, the K -valley of MoSe₂ is aligned with the K' -valley of WS₂. In Fig. 1c we show the spin configuration of the lowest-energy CBs

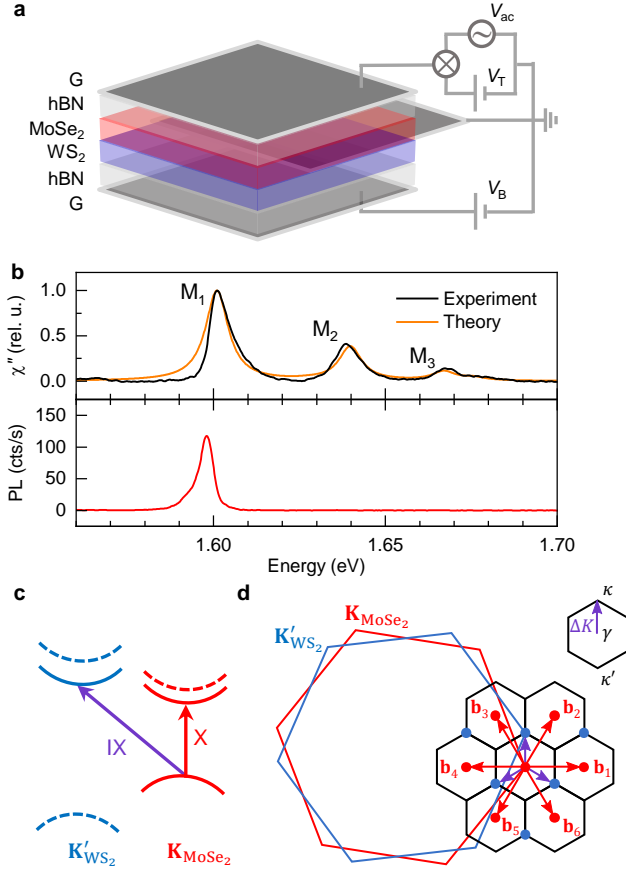


FIG. 1. **a.** Schematics of the MoSe₂/WS₂ heterostructure in a field-effect device, with top and bottom gate voltages V_T and V_B and a small ac-voltage V_{ac} for narrow-band laser modulation spectroscopy. **b.** Top panel: Moiré exciton peaks M_1 , M_2 and M_3 in experimental χ'' as obtained from white light reflection spectra (black) shown together with the theoretical fit (orange). Bottom panel: The PL spectrum is dominated by the lowest-energy state M_1 due to fast population relaxation. **c.** Band structure of antiparallel MoSe₂/WS₂ with spin-polarized subbands indicated by solid and dashed lines, as well as intra- and interlayer excitons. **d.** Mini Brillouin zones with moiré reciprocal vectors \mathbf{b}_j (red arrows) and interlayer coupling (violet arrows). The red and blue points represent intra- and interlayer states considered in the model.

and the highest-energy VBs for the respective valleys of the two layers.

We performed cryogenic white-light differential reflectance (DR) measurements and computed the imaginary part of the dielectric susceptibility χ'' proportional to absorption [27]. In Fig. 1b, we show the spectrum at charge neutrality with three moiré exciton peaks M_1 , M_2 and M_3 . The peak M_1 at 1.60 eV is approximately 30 meV below the monolayer MoSe₂ A-exciton at 1.63 eV and has the largest oscillator strength. The peaks M_2 and M_3 have decreasing oscillator strengths and lie 38 and 65 meV above M_1 , respectively. M_1 is the exciton ground state of the system with bright photolumines-

cence, whereas the higher states are quenched by rapid population relaxation.

The peaks M_1 and M_2 are present in both H- and R-type stackings and have been reported in previous works on MoSe₂/WS₂ [23, 25, 28, 29]. In early studies [25, 28, 30], they have been interpreted as hybridized intra-interlayer excitons and successfully modeled via interlayer tunneling [30, 31]. However, recent experiments on the exciton dispersion in perpendicular electric fields observed vanishing out-of-plane dipoles for both M_1 and M_2 , suggesting that they are of pure intralayer character [23, 29]. While this allows to describe the lowest-energy excitons in terms of a continuum model similarly to WS₂/WSe₂ [32–36], the role of interlayer hybridization remains an open question that we address in this work. Therefore, to describe the complexity of both intra- and interlayer excitons in MoSe₂/WS₂ simultaneously, we first proceed by developing an effective continuum model and subsequently demonstrate its validity by comparison with experimental observations.

We start by developing a phenomenological model combining an intralayer moiré potential with near-resonant interlayer hybridization. The large VB offset between MoSe₂ and WS₂ [24] simplifies the analysis of the lowest-energy spin-bright excitons, and it is sufficient to consider only intralayer excitons (X) of MoSe₂ and interlayer excitons (IX) consisting of a hole in MoSe₂ and an electron in WS₂ (cp. Fig. 1c). The twist angle $\theta \approx 179^\circ$ and the lattice constant mismatch between the two layers result in a small valley mismatch which we denote by $\Delta\mathbf{K} = \mathbf{K}'_{\text{WS}_2} - \mathbf{K}_{\text{MoSe}_2}$. The long-range periodicity of the moiré lattice is reflected by the formation of a mini Brillouin zone (mBZ) [8] with the moiré reciprocal lattice vectors $\mathbf{g}(n, m) = n\mathbf{b}_1 + m\mathbf{b}_2$ shown in Fig. 1d. Here, n and m are integers, $\mathbf{b}_j = (C_6^{j-3} - C_6^{j+1})\Delta\mathbf{K}$ are the first-shell reciprocal lattice vectors, $j = 1, 2, \dots, 6$, and C_6^μ represents rotation by $2\pi\mu/\nu$ (Fig. 1d). We define the angle-dependent mBZ as in Fig. 1d with the center γ matching the K -valley of MoSe₂ ($\mathbf{K}_{\text{MoSe}_2}$), and the point κ at the K' -valley of WS₂ ($\mathbf{K}'_{\text{WS}_2}$).

To define the general moiré Hamiltonian, we introduce two moiré potentials [32–34] for X and IX excitons:

$$V(\mathbf{r}) = \sum_{j=1}^6 V_j \exp(i\mathbf{b}_j \cdot \mathbf{r}),$$

$$W(\mathbf{r}) = \sum_{j=1}^6 W_j \exp(i\mathbf{b}_j \cdot \mathbf{r}).$$

These are the lowest-order harmonic expansions of the moiré potential which, due to the 120° rotational symmetry, present the usual symmetry relations $V_1 = V_3 = V_5 \equiv V$ and $V_2 = V_4 = V_6 \equiv V^*$ (and analogously for W). Restricting ourselves to the low-energy physics of moiré excitons, we assume parabolic dispersions, $E(\mathbf{k}) = E_X + \hbar^2|\mathbf{k}|^2/(2M_X)$ and $\mathcal{E}(\mathbf{k}') = E_{\text{IX}} + \hbar^2|\mathbf{k}'|^2/(2M_{\text{IX}})$.

Here \mathbf{k} and \mathbf{k}' are the center-of-mass wave vectors of X and IX excitons measured from γ and κ , respectively, M_X and M_{IX} are their effective masses, and E_X and E_{IX} are bandgaps averaged over the moiré supercell, resulting in:

$$\langle \mathbf{k} + \mathbf{g}' | H_X | \mathbf{k} + \mathbf{g} \rangle_X = \delta_{\mathbf{g}, \mathbf{g}'} E(\mathbf{k}) + \sum_{j=1}^6 V_j \delta_{\mathbf{g}-\mathbf{g}', \mathbf{b}_j},$$

$$\langle \mathbf{k}' + \mathbf{g}' | H_{IX} | \mathbf{k}' + \mathbf{g} \rangle_{IX} = \delta_{\mathbf{g}, \mathbf{g}'} \mathcal{E}(\mathbf{k}') + \sum_{j=1}^6 W_j \delta_{\mathbf{g}-\mathbf{g}', \mathbf{b}_j}.$$

Notably, V and W do not include resonant interaction terms between X and IX excitons yet, which we introduce explicitly [30] by defining the Hamiltonian as:

$$H = \begin{pmatrix} H_X & T \\ T^* & H_{IX} \end{pmatrix},$$

where the tunneling is described by interlayer hopping elements

$$\langle IX, \mathbf{k}' + \mathbf{g}' | T | X, \mathbf{k} + \mathbf{g} \rangle = \sum_{\eta=0}^2 t \delta_{\mathbf{k}+\mathbf{g}-\mathbf{k}'-\mathbf{g}', C_3^\eta \Delta \mathbf{K}},$$

with the hopping parameter t . We follow the approximation introduced in Refs. [30, 31] and assume the same term t in all mBZs, mediating the hybridization of MoSe₂ excitons X with the closest three IX states in the reciprocal space denoted by the violet arrows in Fig. 1d.

Finally, we restrict the number of vectors \mathbf{g} considered in the Hamiltonian and keep only the lowest seven X-bands and six IX-bands arising from band folding of mBZs as specified by the red and blue dots in Fig. 1d, respectively. Furthermore, we assume that the non-resonant part of the interlayer potential is zero, $W_{1...6} = 0$, resulting in the 13-band Hamiltonian:

$$H(\mathbf{k}) = \begin{pmatrix} E_0 & V & V^* & V & V^* & V & V^* & t & t & t & 0 & 0 & 0 \\ V^* & E_1 & V & 0 & 0 & 0 & V & 0 & 0 & t & 0 & t & 0 \\ V & V^* & E_2 & V^* & 0 & 0 & 0 & t & 0 & 0 & 0 & 0 & t \\ V^* & 0 & V & E_3 & V & 0 & 0 & t & 0 & 0 & 0 & 0 & t \\ V & 0 & 0 & V^* & E_4 & V^* & 0 & 0 & t & 0 & 0 & 0 & t \\ V^* & 0 & 0 & 0 & V & E_5 & V & 0 & t & 0 & t & 0 & 0 \\ V & V^* & 0 & 0 & 0 & V^* & E_6 & 0 & 0 & t & t & 0 & 0 \\ t^* & 0 & t^* & t^* & 0 & 0 & 0 & \mathcal{E}_0 & 0 & 0 & 0 & 0 & 0 \\ t^* & 0 & 0 & 0 & t^* & t^* & 0 & 0 & \mathcal{E}_1 & 0 & 0 & 0 & 0 \\ t^* & t^* & 0 & 0 & 0 & 0 & t^* & 0 & 0 & \mathcal{E}_2 & 0 & 0 & 0 \\ 0 & 0 & 0 & 0 & 0 & t^* & t^* & 0 & 0 & 0 & \mathcal{E}_3 & 0 & 0 \\ 0 & t^* & t^* & 0 & 0 & 0 & 0 & 0 & 0 & 0 & 0 & \mathcal{E}_4 & 0 \\ 0 & 0 & 0 & t^* & t^* & 0 & 0 & 0 & 0 & 0 & 0 & 0 & \mathcal{E}_5 \end{pmatrix}. \quad (1)$$

The first seven diagonal terms correspond to the X bands marked by the red dots in Fig. 1d, with

$$E_0(\mathbf{k}) = E(\mathbf{k}), \quad E_j(\mathbf{k}) = E(\mathbf{k} - \mathbf{b}_j),$$

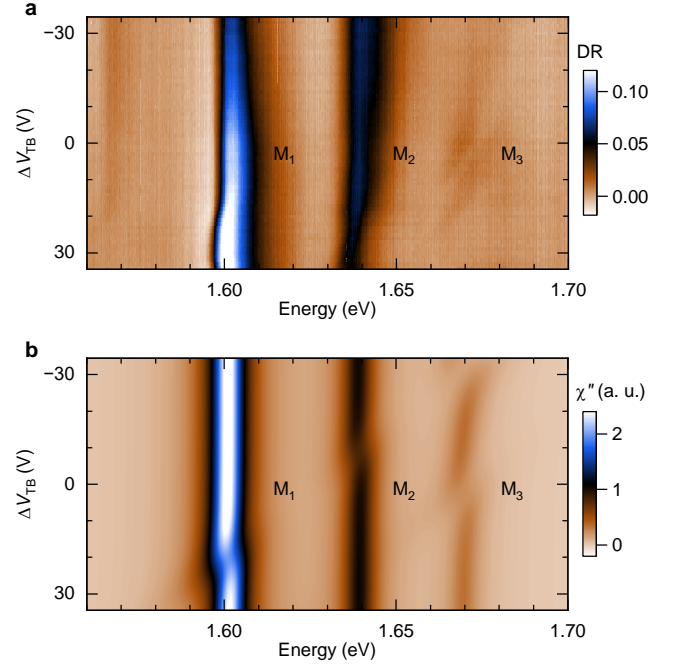


FIG. 2. **a.** Experimental DR signal of MoSe₂/WS₂ as a function of the out-of-plane electric field. **b.** Corresponding simulation of $\chi''(\omega)$ capturing the strong intralayer character of the three lowest-energy moiré exciton peaks as well as their relative strengths. Inhomogeneous broadening was included by smoothing $\chi''(\omega)$ over a 5 meV broad Gaussian kernel in the fit parameter E_{IX} .

for $j = 1, 2, \dots, 6$; the last six diagonal terms relate to IXs marked by the blue dots in Fig. 1d:

$$\mathcal{E}_\eta(\mathbf{k}) = \mathcal{E}(\mathbf{k} - C_3^\eta \Delta \mathbf{K}), \quad \mathcal{E}_\zeta(\mathbf{k}) = \mathcal{E}(\mathbf{k} + 2C_3^{\zeta-3} \Delta \mathbf{K}), \quad (2)$$

where $\eta = 0, 1, 2$ and $\zeta = 3, 4, 5$. This Hamiltonian combines the non-resonant intralayer continuum model described by the potential V [32–34] with the interlayer hybridization described by the hopping parameter t [27, 30, 31], and it can be used to compute the band dispersion within the full mBZ. Here, since we are mainly interested in the optical response of the system, we consider the center of the mBZ at the γ -point. After diagonalization of the Hamiltonian in Eq. (1), we obtain χ'' by projecting the eigenstates onto the fundamental A-exciton state as:

$$\chi''(\omega) \approx \chi_0'' \sum_{m=1}^{13} | \langle m | A \rangle |^2 \frac{\gamma_0^2}{\hbar^2 (\omega - \omega_m)^2 + \gamma_0^2}, \quad (3)$$

where $|A\rangle$ is the MoSe₂ intralayer exciton state corresponding to the first row and column in Eq. (1), χ_0'' is its dielectric susceptibility [32], $|m\rangle$ and $\hbar\omega_m$ are the eigenstates and eigenvalues of the m -th exciton band obtained from the diagonalized Hamiltonian in Eq. (1), and γ_0 is a peak broadening parameter. Notably, this implies that the oscillator strength of the $|A\rangle$ exciton is redistributed among the set of the moiré excitons $|m\rangle$.

By fitting the model to electric field dependent data shown below (Figs. 2 and 3) we reproduce the multiplicity and relative oscillator strengths of the three moiré excitons with very good agreement. In Fig. 1b we show the theoretical χ'' obtained for the material parameters $a_{\text{MoSe}_2} = 0.3288$ nm, $a_{\text{WS}_2} = 0.3154$ nm, $M_X = 1.44m_0$, and $M_{\text{IX}} = 0.86m_0$ [37, 38] with electron mass m_0 , and with free fitting parameters $E_X = 1617$ meV, $E_{\text{IX}} = 1614$ meV, $\theta = 178.8^\circ$, $|V| = 9.3$ meV, $\arg(V) = \pi/5$, $t = 3$ meV and $\gamma_0 = 4$ meV. We emphasize that although $E_{\text{IX}} < E_X$, the fitting implies a type I heterostructure due to the relation $E_{\text{IX}} > \min[E_X + V(\mathbf{r})] \approx 1566$ meV, with a CB offset in the order of 50 meV. The remaining fit parameters for a given twist angle ($|V|$, $\arg(V)$, and t) determine the layer character of moiré excitons as well as their energy separations and oscillator strengths.

The validity of the model is best seen by comparison with the data in Fig. 2a showing the evolution of DR with an out-of-plane electric field proportional to ΔV_{TB} . As already pointed out in previous studies [23, 29], the peaks M_1 and M_2 behave as intralayer states with vanishingly small linear slopes of the first-order Stark effect. For these peaks, this implies that they can be captured in terms of the non-resonant moiré potential V , whereas interlayer tunneling plays a negligible role. The peak M_3 , on the contrary, exhibits two branches with finite dispersion indicative of an anticrossing of X and IX states with weak coupling, which necessitates a non-vanishing hopping parameter t in the model. Also, M_1 and M_2 show minor narrowing with a small red-shift at high $\Delta V_{\text{TB}} \geq 18$ V, indicating the presence of dark IX resonances.

To describe this behavior we compute the evolution of $\chi''(\omega)$ as a function of ΔV_{TB} by shifting the IX resonance energies in (2) as

$$\mathcal{E}(\Delta V_{\text{TB}}) = \mathcal{E} - \frac{ed\Delta V_{\text{TB}}}{\epsilon l}, \quad (4)$$

where e is the electron charge, $d = 0.6$ nm the distance between the two TMD layers, $l = 110$ nm the distance between the gates, and $\epsilon \approx 4$ [39]. The resulting susceptibility, plotted in Fig. 2b, captures the main features of the experimental data such as the relative strengths of the peaks, the strong intralayer character of M_1 and M_2 , the anticrossing of the M_3 doublet and the IX perturbation of M_1 at high positive fields. At the same time, it predicts a weak coupling of M_2 with an IX state at $\Delta V_{\text{TB}} \approx -10$ V which can not be observed in white-light DR.

To improve the sensitivity to interlayer states we repeated the field-dependent measurement with the modulation-spectroscopy technique – an approach that uses a narrow-band tunable laser to measure differential reflectance DR' [40–42]. The measurement is performed by modulating one of the gates of the device by a small ac-voltage (V_{ac} in Fig. 1a) and using a lock-in ampli-

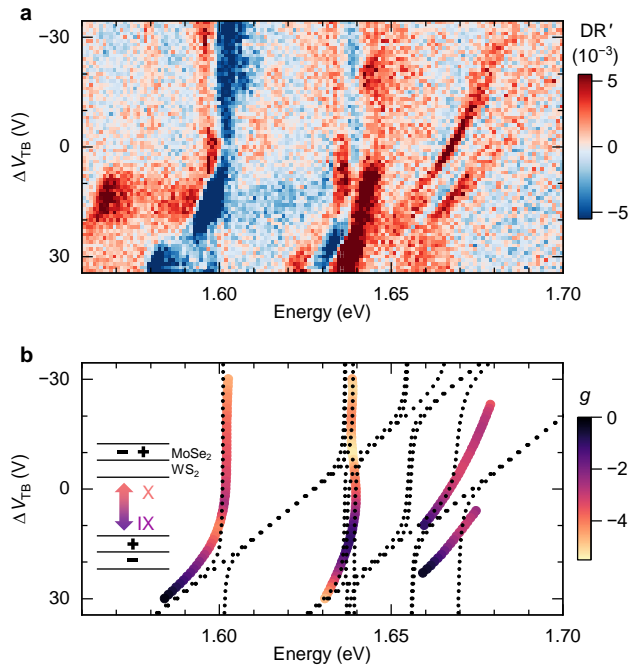


FIG. 3. **a.** Narrow-band modulation spectroscopy signal of MoSe₂/WS₂ as a function of the applied out-of-plane electric field. **b.** Dispersion of the eigenvalues of the Hamiltonian in Eq. (1) as a function of the electric field and experimental exciton g -factors of the respective resonances color-coded from -5.5 (yellow) to 0 (black) .

fier to detect the reflected signal at the same frequency, R_{ac} , simultaneously with the dc part of the photosignal, R_{dc} [27]. In Fig. 3a we show $\text{DR}' = R_{\text{ac}}/R_{\text{dc}}$ with signatures of both intra- and interlayer states: the interlayer character of the M_3 doublet becomes much more prominent compared to the white-light DR data, the red-shifts of M_1 and M_2 at high ΔV_{TB} confirm the admixing of IX excitons, and the contrast change of M_2 at $\Delta V_{\text{TB}} \approx -20$ V suggests the coupling to a dark IX state made visible with this technique.

In Fig. 3b we show the dispersion of the peaks extracted from Fig. 3a alongside the evolution of the eigenvalues of the Hamiltonian in Eq. (1) as a function of ΔV_{TB} . In contrast to Fig. 2b, where the oscillator strengths of the three bright excitons are visible, here the dotted lines indicate the eigenvalues corresponding to all 13 moiré exciton bands irrespective of their oscillator strength. The experimental dispersion of both M_1 and M_2 in Fig. 3a is well reproduced, and the strong anticrossing of the M_3 doublet [27] is qualitatively captured within our theoretical model. We note that although the magnitude of the X-IX coupling changes between the M_2 and M_3 resonances, they are both controlled by the same parameter t , and introducing different hopping parameters for different mBZs [29] would allow to improve on the quantitative agreement with the data. Finally, we find that in the neutral regime the first IX state – which

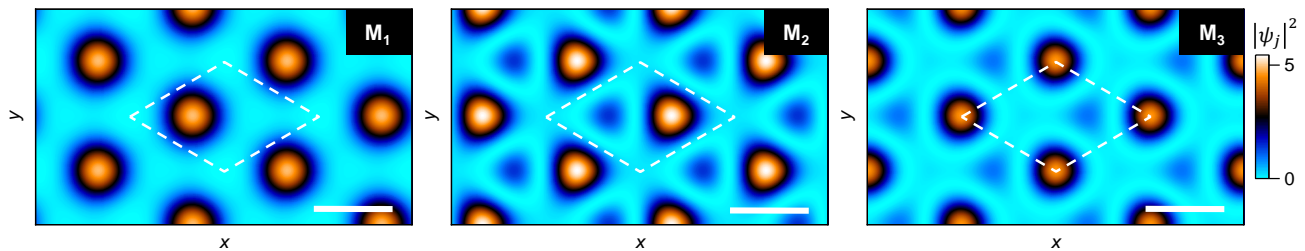


FIG. 4. Spatial distribution of the exciton wavefunction for the three lowest-energy bright states M_1 , M_2 and M_3 (all scale-bars are 5 nm). All three states are located in different positions of the moiré supercell delimited by the dashed lines.

is momentum-dark and can not be observed in Fig. 2 – lies 30 meV above the ground state M_1 , indicating type I character for the studied MoSe₂/WS₂ heterostack.

Additionally to the electric field dependence we studied the Zeeman effect of moiré excitons by repeating the modulation-spectroscopy measurements for out-of-plane magnetic fields in the range of $B = \pm 6T$ [27]. The colors of the data in Fig. 3b show the g -factors of the respective peaks for different electric fields, ranging from $g = -5.5$ (yellow) through -2 (purple) to 0 (black). We observe that for electric fields where M_1 and M_2 follow vertical lines of zero Stark effect due to nearly-pure MoSe₂ character, the corresponding g -factors are close to the fundamental MoSe₂ A-exciton with $g_A \approx -4$. Near the IX-X anticrossings, on the contrary, all three states exhibit sizable changes in the g -factors reaching values up to 0 . The effect is most pronounced for the dispersive branch of M_1 at high positive electric fields as well as the M_3 doublet, which we attribute to field-induced hybridization with interlayer states. The values of the exciton g -factors depend on both the degree of layer hybridization and the exciton momentum [43, 44], making a full quantitative description of this behavior out of scope for this work. The overall trend, however, is consistent with the intralayer character of the peaks M_1 and M_2 at negative electric fields, and with interlayer admixing near anticrossings captured by our theoretical model.

Finally, for zero electric and magnetic fields, we illustrate the difference of the three bright moiré excitons by plotting the spatial distributions of their wavefunctions in Fig. 4 [27]. Remarkably, all three states are located at different points of the moiré supercell and exhibit different spatial distributions: the ground state exciton M_1 is tightly localized, whereas both M_2 and M_3 have non-negligible spatial extents. We note that a detailed modeling of such behavior requires the explicit knowledge of both the electron and the hole potential [45], whereas in our model, the spatial characteristics of moiré excitons are captured entirely through the exciton potential V .

In summary, our work demonstrates that due to the close CB alignment between MoSe₂ and WS₂, full description of moiré exciton phenomena requires exciton mixing from a non-resonant moiré potential as well as

resonant interlayer hybridization. We provide a simple model that highlights the importance of both effects and accurately captures the main experimental observations, and which general applicability will open avenues for future studies in related two-dimensional moiré structures with significance of both intra- and interlayer effects.

We acknowledge funding by the European Research Council (ERC) under the Grant Agreement No. 772195 as well as the Deutsche Forschungsgemeinschaft (DFG, German Research Foundation) within the Priority Programme SPP 2244 2DMP and the Germany’s Excellence Strategy EXC-2111-390814868. B.P. acknowledges funding by IMPRS-QST. S.M. and I.B. acknowledge support from the Alexander von Humboldt Foundation. X.H. and A.S.B. received funding from the European Union’s Framework Programme for Research and Innovation Horizon 2020 (2014–2020) under the Marie Skłodowska-Curie Grant Agreement No. 754388 (LMUResearchFellows) and from LMUexcellent, funded by the Federal Ministry of Education and Research (BMBF) and the Free State of Bavaria under the Excellence Strategy of the German Federal Government and the Länder. Z.L. was supported by the China Scholarship Council (CSC), No. 201808140196. K.W. and T.T. acknowledge support from JSPS KAKENHI (Grant Numbers 19H05790, 20H00354 and 21H05233).

B. P., J. S., and S. M. contributed equally to this work.

* borislav.polovnikov@physik.lmu.de

† alexander.hoegele@lmu.de

‡ anvar.baimuratov@lmu.de

- [1] G. Wang, A. Chernikov, M. M. Glazov, T. F. Heinz, X. Marie, T. Amand, and B. Urbaszek, Colloquium: Excitons in atomically thin transition metal dichalcogenides, *Rev. Mod. Phys.* **90**, 021001 (2018).
- [2] M. Koperski, M. R. Molas, A. Arora, K. Nogajewski, A. O. Slobodeniuk, C. Faugeras, and M. Potemski, Optical properties of atomically thin transition metal dichalcogenides: observations and puzzles, *Nanophotonics* **6**, 1289 (2017).
- [3] S. Manzeli, D. Ovchinnikov, D. Pasquier, O. V. Yazyev,

- and A. Kis, 2D transition metal dichalcogenides, *Nat. Rev. Mater.* **2**, 1 (2017).
- [4] A. K. Geim and I. V. Grigorieva, Van der Waals heterostructures, *Nature* **499**, 419 (2013).
- [5] L. Balents, C. R. Dean, D. K. Efetov, and A. F. Young, Superconductivity and strong correlations in moiré flat bands, *Nat. Phys.* **16**, 725 (2020).
- [6] R. Bistritzer and A. H. MacDonald, Moiré bands in twisted double-layer graphene, *Proc. Natl. Acad. Sci. U.S.A.* **108**, 12233 (2011).
- [7] K. F. Mak and J. Shan, Semiconductor moiré materials, *Nat. Nanotechnol.* **17**, 686 (2022).
- [8] K. Hermann, Periodic overlayers and moiré patterns: theoretical studies of geometric properties, *J. Phys.: Condens. Matter* **24**, 314210 (2012).
- [9] R. Ribeiro-Palau, C. Zhang, K. Watanabe, T. Taniguchi, J. Hone, and C. R. Dean, Twistable electronics with dynamically rotatable heterostructures, *Science* **361**, 690 (2018).
- [10] N. P. Wilson, W. Yao, J. Shan, and X. Xu, Excitons and emergent quantum phenomena in stacked 2D semiconductors, *Nature* **599**, 383 (2021).
- [11] D. Huang, J. Choi, C.-K. Shih, and X. Li, Excitons in semiconductor moiré superlattices, *Nat. Nanotechnol.* **17**, 227 (2022).
- [12] Y. Tang, L. Li, T. Li, Y. Xu, S. Liu, K. Barmak, K. Watanabe, T. Taniguchi, A. H. MacDonald, J. Shan, and K. F. Mak, Simulation of Hubbard model physics in WSe_2/WSe_2 moiré superlattices, *Nature* **579**, 353 (2020).
- [13] A. J. Campbell, M. Brotons-Gisbert, H. Baek, V. Vitale, T. Taniguchi, K. Watanabe, J. Lischner, and B. D. Gerardot, Exciton-polarons in the presence of strongly correlated electronic states in a $MoSe_2/WSe_2$ moiré superlattice, *npj 2D Mater. Appl.* **6**, 1 (2022).
- [14] E. C. Regan, D. Wang, C. Jin, M. I. Bakti Utama, B. Gao, X. Wei, S. Zhao, W. Zhao, Z. Zhang, K. Yumigeta, M. Blei, J. D. Carlström, K. Watanabe, T. Taniguchi, S. Tongay, M. Crommie, A. Zettl, and F. Wang, Mott and generalized Wigner crystal states in WSe_2/WSe_2 moiré superlattices, *Nature* **579**, 359 (2020).
- [15] Y. Zhou, J. Sung, E. Brutschea, I. Esterlis, Y. Wang, G. Scuri, R. J. Gelly, H. Heo, T. Taniguchi, K. Watanabe, G. Zaránd, M. D. Lukin, P. Kim, E. Demler, and H. Park, Bilayer wigner crystals in a transition metal dichalcogenide heterostructure, *Nature* **595**, 48 (2021).
- [16] Y. Shimazaki, I. Schwartz, K. Watanabe, T. Taniguchi, M. Kroner, and A. Imamoğlu, Strongly correlated electrons and hybrid excitons in a moiré heterostructure, *Nature* **580**, 472 (2020).
- [17] L. Wang, E.-M. Shih, A. Ghiotto, L. Xian, D. A. Rhodes, C. Tan, M. Claassen, D. M. Kennes, Y. Bai, B. Kim, K. Watanabe, T. Taniguchi, X. Zhu, J. Hone, A. Rubio, A. N. Pasupathy, and C. R. Dean, Correlated electronic phases in twisted bilayer transition metal dichalcogenides, *Nat. Mater.* **19**, 861 (2020).
- [18] X. Huang, T. Wang, S. Miao, C. Wang, Z. Li, Z. Lian, T. Taniguchi, K. Watanabe, S. Okamoto, D. Xiao, S.-F. Shi, and Y.-T. Cui, Correlated insulating states at fractional fillings of the WS_2/WSe_2 moiré lattice, *Nat. Phys.* **17**, 715 (2021).
- [19] A. Ghiotto, E.-M. Shih, G. S. S. G. Pereira, D. A. Rhodes, B. Kim, J. Zang, A. J. Millis, K. Watanabe, T. Taniguchi, J. C. Hone, L. Wang, C. R. Dean, and A. N. Pasupathy, Quantum criticality in twisted transition metal dichalcogenides, *Nature* **597**, 345 (2021).
- [20] Y. Xu, S. Liu, D. A. Rhodes, K. Watanabe, T. Taniguchi, J. Hone, V. Elser, K. F. Mak, and J. Shan, Correlated insulating states at fractional fillings of moiré superlattices, *Nature* **587**, 214 (2020).
- [21] T. Li, S. Jiang, L. Li, Y. Zhang, K. Kang, J. Zhu, K. Watanabe, T. Taniguchi, D. Chowdhury, L. Fu, J. Shan, and K. F. Mak, Continuous Mott transition in semiconductor moiré superlattices, *Nature* **597**, 350 (2021).
- [22] T. Li, J. Zhu, Y. Tang, K. Watanabe, T. Taniguchi, V. Elser, J. Shan, and K. F. Mak, Charge-order-enhanced capacitance in semiconductor moiré superlattices, *Nat. Nanotechnol.* **16**, 1068 (2021).
- [23] Y. Tang, J. Gu, S. Liu, K. Watanabe, T. Taniguchi, J. C. Hone, K. F. Mak, and J. Shan, Dielectric catastrophe at the Wigner-Mott transition in a moiré superlattice, *Nat. Commun.* **13**, 1 (2022).
- [24] C. Zhang, C. Gong, Y. Nie, K.-A. Min, C. Liang, Y. J. Oh, H. Zhang, W. Wang, S. Hong, L. Colombo, R. M. Wallace, and K. Cho, Systematic study of electronic structure and band alignment of monolayer transition metal dichalcogenides in van der Waals heterostructures, *2D Mater.* **4**, 015026 (2016).
- [25] L. Zhang, Z. Zhang, F. Wu, D. Wang, R. Gogna, S. Hou, K. Watanabe, T. Taniguchi, K. Kulkarni, T. Kuo, S. R. Forrest, and H. Deng, Twist-angle dependence of moiré excitons in $WS_2/MoSe_2$ heterobilayers, *Nat. Commun.* **11**, 5888 (2020).
- [26] I. Bilgin, F. Liu, A. Vargas, A. Winchester, M. K. Man, M. Upmanyu, K. M. Dani, G. Gupta, S. Talapatra, A. D. Mohite, and S. Kar, Chemical vapor deposition synthesized atomically thin molybdenum disulfide with optoelectronic-grade crystalline quality, *ACS Nano* **9**, 8822 (2015).
- [27] See Supplemental Material for descriptions of the device layout and fabrication, the computation of χ'' from DR data, the measurement setup, the limiting cases of the theoretical model, its dependence on individual parameters and the computation of the exciton wavefunctions, which includes Refs. [40, 46-48]
- [28] E. M. Alexeev, D. A. Ruiz-Tijerina, M. Danovich, M. J. Hamer, D. J. Terry, P. K. Nayak, S. Ahn, S. Pak, J. Lee, J. I. Sohn, M. R. Molas, M. Koperski, K. Watanabe, T. Taniguchi, K. S. Novoselov, R. V. Gorbachev, H. S. Shin, V. I. Fal'ko, and A. I. Tartakovskii, Resonantly hybridized excitons in moiré superlattices in van der Waals heterostructures, *Nature* **567**, 81 (2019).
- [29] Y. Tang, J. Gu, S. Liu, K. Watanabe, T. Taniguchi, J. Hone, K. F. Mak, and J. Shan, Tuning layer-hybridized moiré excitons by the quantum-confined Stark effect, *Nat. Nanotechnol.* **16**, 52 (2021).
- [30] D. A. Ruiz-Tijerina and V. I. Fal'ko, Interlayer hybridization and moiré superlattice minibands for electrons and excitons in heterobilayers of transition-metal dichalcogenides, *Phys. Rev. B* **99**, 125424 (2019).
- [31] Y. Wang, Z. Wang, W. Yao, G.-B. Liu, and H. Yu, Interlayer coupling in commensurate and incommensurate bilayer structures of transition-metal dichalcogenides, *Phys. Rev. B* **95**, 115429 (2017).
- [32] F. Wu, T. Lovorn, and A. H. MacDonald, Topological Exciton Bands in Moiré Heterojunctions, *Phys. Rev. Lett.* **118**, 147401 (2017).
- [33] F. Wu, T. Lovorn, and A. H. MacDonald, Theory of op-

- tical absorption by interlayer excitons in transition metal dichalcogenide heterobilayers, *Phys. Rev. B* **97**, 035306 (2018).
- [34] F. Wu, T. Lovorn, E. Tutuc, and A. H. MacDonald, Hubbard model physics in transition metal dichalcogenide moiré bands, *Phys. Rev. Lett.* **121**, 026402 (2018).
- [35] K. Tran, G. Moody, F. Wu, X. Lu, J. Choi, K. Kim, A. Rai, D. A. Sanchez, J. Quan, A. Singh, J. Embley, A. Zepeda, M. Campbell, T. Autry, T. Taniguchi, K. Watanabe, N. Lu, S. K. Banerjee, K. L. Silverman, S. Kim, E. Tutuc, L. Yang, A. H. MacDonald, and X. Li, Evidence for moiré excitons in van der Waals heterostructures, *Nature* **567**, 71 (2019).
- [36] C. Jin, E. C. Regan, A. Yan, M. Iqbal Bakti Utama, D. Wang, S. Zhao, Y. Qin, S. Yang, Z. Zheng, S. Shi, K. Watanabe, T. Taniguchi, S. Tongay, A. Zettl, and F. Wang, Observation of moiré excitons in WSe₂/WS₂ heterostructure superlattices, *Nature* **567**, 76 (2019).
- [37] A. Kormányos, G. Burkard, M. Gmitra, J. Fabian, V. Zólyomi, N. D. Drummond, and V. Fal'ko, k-p theory for two-dimensional transition metal dichalcogenide semiconductors, *2D Mater.* **2**, 022001 (2015).
- [38] M. Goryca, J. Li, A. V. Stier, T. Taniguchi, K. Watanabe, E. Courtade, S. Shree, C. Robert, B. Urbaszek, X. Marie, and S. A. Crooker, Revealing exciton masses and dielectric properties of monolayer semiconductors with high magnetic fields, *Nat. Commun.* **10**, 1 (2019).
- [39] Z. Wang, Y.-H. Chiu, K. Honz, K. F. Mak, and J. Shan, Electrical Tuning of Interlayer Exciton Gases in WSe₂ Bilayers, *Nano Lett.* **18**, 137 (2018).
- [40] B. Alén, F. Bickel, K. Karrai, R. J. Warburton, and P. M. Petroff, Stark-shift modulation absorption spectroscopy of single quantum dots, *Appl. Phys. Lett.* **83**, 2235 (2003).
- [41] A. Högele, B. Alén, F. Bickel, R. J. Warburton, P. M. Petroff, and K. Karrai, Exciton fine structure splitting of single InGaAs self-assembled quantum dots, *Physica E* **21**, 175 (2004).
- [42] E. Barré, O. Karni, E. Liu, A. L. O'Beirne, X. Chen, H. B. Ribeiro, L. Yu, B. Kim, K. Watanabe, T. Taniguchi, K. Barmak, C. H. Lui, S. Refaely-Abramson, F. H. da Jornada, and T. F. Heinz, Optical absorption of interlayer excitons in transition-metal dichalcogenide heterostructures, *Science* **376**, 406 (2022).
- [43] P. E. Faria Junior and J. Fabian, Signatures of electric field and layer separation effects on the spin-valley physics of mose₂/wse₂ heterobilayers: From energy bands to dipolar excitons, *Nanomaterials* **13**, 10.3390/nano13071187 (2023).
- [44] Y. G. Gobato, C. S. de Brito, A. Chaves, M. A. Prosnikov, T. Woźniak, S. Guo, I. D. Barcelos, M. V. Milošević, F. Withers, and P. C. M. Christianen, Distinctive g-Factor of Moiré-Confined Excitons in van der Waals Heterostructures, *Nano Lett.* **22**, 8641 (2022).
- [45] M. H. Naik, E. C. Regan, Z. Zhang, Y.-H. Chan, Z. Li, D. Wang, Y. Yoon, C. S. Ong, W. Zhao, S. Zhao, M. I. B. Utama, B. Gao, X. Wei, M. Sayyad, K. Yumigeta, K. Watanabe, T. Taniguchi, S. Tongay, F. H. da Jornada, F. Wang, and S. G. Louie, Intralayer charge-transfer moiré excitons in van der Waals superlattices, *Nature* **609**, 52 (2022).
- [46] A. Arora, A. Mandal, S. Chakrabarti, and S. Ghosh, Magneto-optical Kerr effect spectroscopy based study of Landé g-factor for holes in GaAs/AlGaAs single quantum wells under low magnetic fields, *J. Appl. Phys.* **113**, 213505 (2013).
- [47] S. Zhao, Z. Li, X. Huang, A. Rupp, J. Göser, I. A. Vovk, S. Yu. Kruchinin, K. Watanabe, T. Taniguchi, I. Bilgin, A. S. Baimuratov, and A. Högele, Excitons in mesoscopically reconstructed moiré heterostructures, *Nat. Nanotechnol.* **18**, 572 (2023).
- [48] J. D. E. McIntyre and D. E. Aspnes, Differential reflection spectroscopy of very thin surface films, *Surf. Sci.* **24**, 417 (1971).

Supplementary Material: Field-induced hybridization of moiré excitons in MoSe₂/WS₂ heterobilayers

Borislav Polovnikov, Johannes Scherzer, Subhadeep Misra, Xin Huang, Christian Mohl, Zhijie Li, Jonas Göser, Jonathan Förste, Ismail Bilgin, Kenji Watanabe, Takashi Taniguchi, Alexander Högele, and Anvar S. Baimuratov

DEVICE LAYOUT AND FABRICATION

We obtained monolayers of MoSe₂ and WS₂ from in-house CVD synthesis. Thin flakes of hBN were exfoliated from bulk crystals provided by NIMS, Japan. All flakes were then stacked together by the dry-transfer technique using PDMS/PC stamps, deposited onto a Si/SiO₂ substrate and annealed at 200°C for 12 hours. Given the triangular shape of CVD-grown TMD crystals we controlled the relative orientation of the two crystals and fabricated an H-type sample (anti parallel alignment) with a rotation angle of ca. 179°, see Fig. S1.

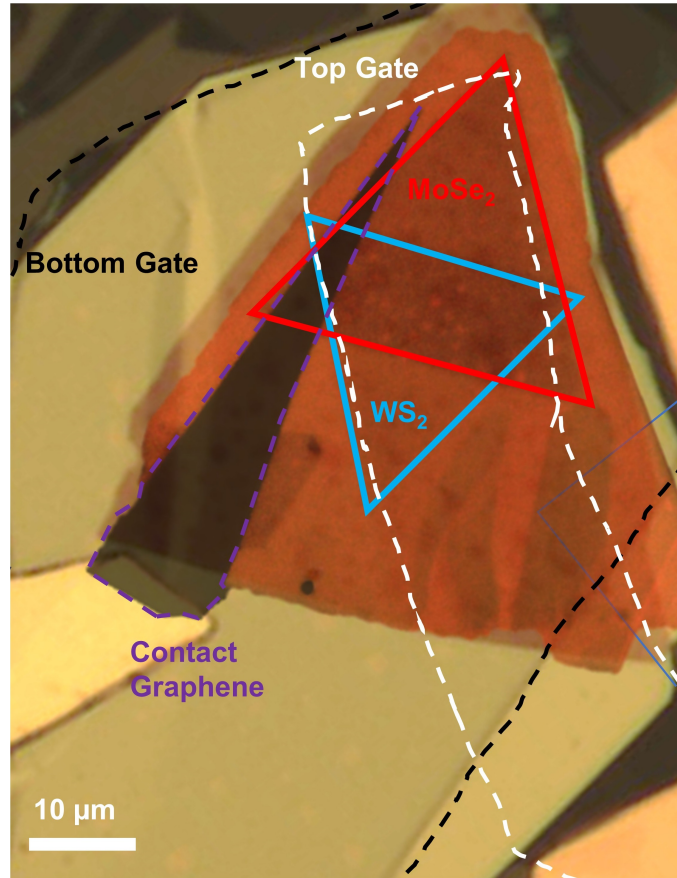


FIG. S1. Optical image of the studied MoSe₂/WS₂ device. The triangular single-crystal monolayers of MoSe₂ and WS₂ have a twist angle of approximately 179° and are delimited in red and blue. The few-layer graphite flakes used for the electric gates are delimited by dashed lines.

CALCULATION OF THE ABSORPTION COEFFICIENT χ''

For comparison between measurements and theory we translate the differential reflectance (DR) signal into the imaginary part of the dielectric susceptibility $\chi = \chi' + i\chi''$ by following Refs. 1 and 2. We define DR as $(R_0 - R)/R_0$, where R is the reflectance signal from the sample and R_0 is a reference background signal from the substrate. As pointed out in [3], without hBN encapsulation the DR signal would simply be proportional to χ'' . In the present device, however, the top and bottom hBN (both of 55 nm thickness) add additional interfaces that influence the lineshape of the reflected signal by interference effects. As shown in [1], these effects can be taken into account by introducing a phenomenological phase factor for the effective susceptibility $\tilde{\chi} = \chi e^{i\alpha}$, where α is an *a priori* wavelength-dependent phase factor and the DR signal is now proportional to the imaginary part of $\tilde{\chi}$, $\text{DR} \sim \text{Im}(\tilde{\chi})$. Here, for simplicity, we assume α to be a constant in the relevant spectral range. Then, using the Kramers-Kronig relations for the complex-valued function $\tilde{\chi}(\omega)$, we can compute χ'' from DR as

$$\chi''(\omega) = \text{Im} (e^{-i\alpha} \tilde{\chi}(\omega)) = \cos(\alpha) \text{DR}(\omega) - \sin(\alpha) \int_{\mathbb{R}} \frac{\text{DR}(\omega')}{\omega - \omega'} d\omega'. \quad (1)$$

In Fig. S2 we plot the raw DR signal corresponding to the data shown in Fig. 1b of the main text ($\alpha = 0^\circ$) alongside the phase-corrected data ($\alpha = 13^\circ$) and a third example with an arbitrary phase for illustration of the principle ($\alpha = -45^\circ$). The phase which was used in the main text is chosen such that the individual moiré exciton peaks exhibit almost lorentzian lineshape, as expected for the absorption of individual exciton resonances.

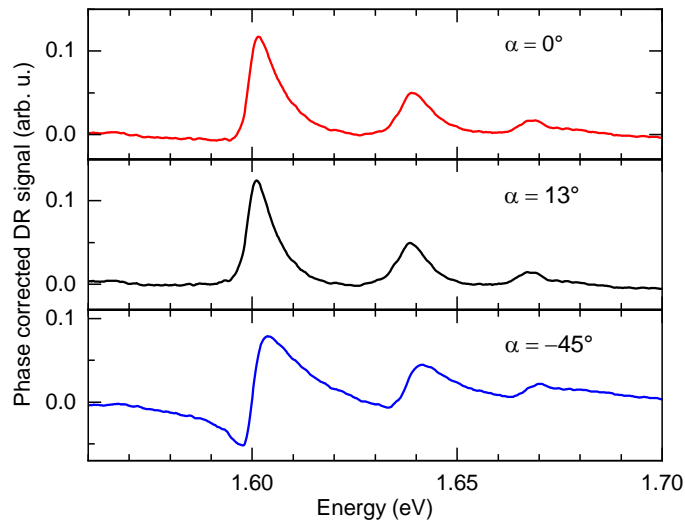


FIG. S2. Top: Raw DR signal corresponding to the data shown in Fig. 1b of the main text. Middle: Phase corrected DR with the phase $\alpha = 13^\circ$ which was used in the main text. Bottom: Phase corrected DR with $\alpha = -45^\circ$.

EXPERIMENTAL SETUP

Cryogenic spectroscopy was conducted using home-built confocal microscopes in back-scattering geometry. The sample was loaded into a closed-cycle cryostat (attocube systems, attoDRY1000) with a base temperature of 3.2 K equipped with a superconducting magnet providing magnetic fields of up to ± 9 T in Faraday configuration. Piezo-stepping and scanning units (attocube systems, ANPxyz and ANSxy100) were used for sample positioning with respect to a low-temperature apochromatic objective (attocube systems).

For PL and white light DR, the signal was spectrally dispersed by a monochromator (Acton SP2500 with a 300 grooves/mm grating) and detected by a liquid nitrogen cooled charge-coupled device (Spec-10:100BR). A set of linear polarizers (Thorlabs, LPVIS), half- and quarter-waveplates (B. Halle, 310 – 1100 nm achromatic) mounted on piezo-rotators (attocube systems, ANR240) were used to control the polarization in excitation and detection. A wavelength-tunable Ti:sapphire laser (Mira) in continuous-wave mode and laser diodes were used to excite PL. For DR

measurements, a stabilized Tungsten-Halogen lamp (Thorlabs, SLS201L) and supercontinuum lasers (NKT Photonics, SuperK Extreme and SuperK Varia) were used as broadband light sources.

For narrow band modulation spectroscopy, a wavelength-tunable Ti:sapphire laser (M squared) of $50 \mu\text{eV}$ linewidth was used to excite the sample while modulating the top gate with an ac-voltage $V_{ac} = 500 \text{ mV}$ at 147 Hz . The reflected optical signal was detected by a silicon photodiode and its output was preamplified by Ithaco Model 1211. The amplified dc part of the photosignal (R_{dc}) was measured, and the ac part was demodulated and amplified further by lock-in amplifier (EG&G 7260), supplied with the reference frequency same as that of the modulation voltage to obtain R_{ac} (see Fig. S3). Finally, the *narrow-band differential reflectance* (DR') is given by the ratio of the demodulated ac part to the dc photosignal, R_{ac}/R_{dc} . An integration time constant of 1 s was used per data point acquisition. In simple limits of the modulation conditions, the signal is proportional to the derivative of DR [4], whereas in general, it requires a microscopic analysis including optical pumping of charge carrier reservoirs.

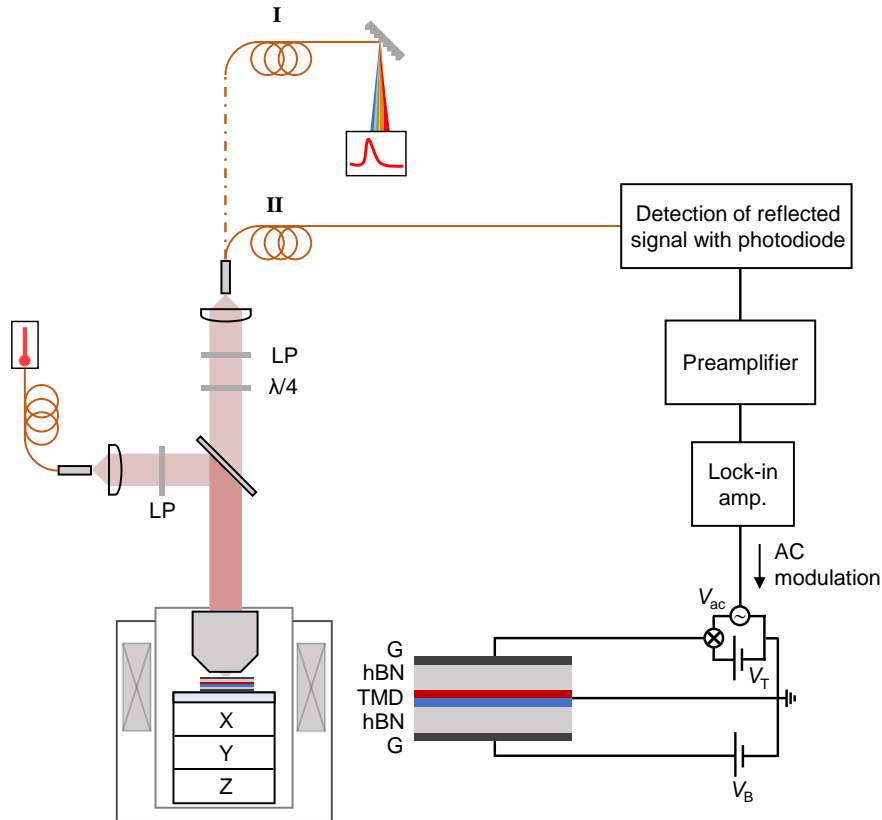


FIG. S3. Experimental setup for PL and DR measurements (I) and for narrow band modulation spectroscopy (II). The sample is mounted on a stack of piezo positioners (X/Y/Z) inside a closed-cycle cryostat at a base temperature of 3.2 K . A home built, fiber-based confocal microscope with an apochromatic objective is used to focus the excitation light (horizontal microscope arm) onto the sample, and the reflected/emitted light is then collected by the same objective and coupled into the detection fiber (vertical microscope arm). The light from the detection fiber is either dispersed by a monochromator for spectral information (I), or detected by a silicon photodiode for narrow-band modulation measurements (II). A set of linear polarizers (LP), waveplates ($\lambda/4$) and optionally also optical filters is used to control the incident light.

MEASUREMENT OF EXCITON g -FACTORS

To measure the g -factors shown in Fig. 3b of the main text, we repeated the narrow-band modulation spectroscopy measurement for a series of out-of-plane magnetic fields between $B = 6$ T and $B = -6$ T. The measurements were performed under linearly polarized excitation with detection in both σ^+ and σ^- polarization. The valley Zeeman energy splitting ΔE between the two polarization branches was obtained from the peak-maxima energies, and the g -factor was extracted from the slope of the best linear fit of ΔE as a function of B as shown in Fig. S4.

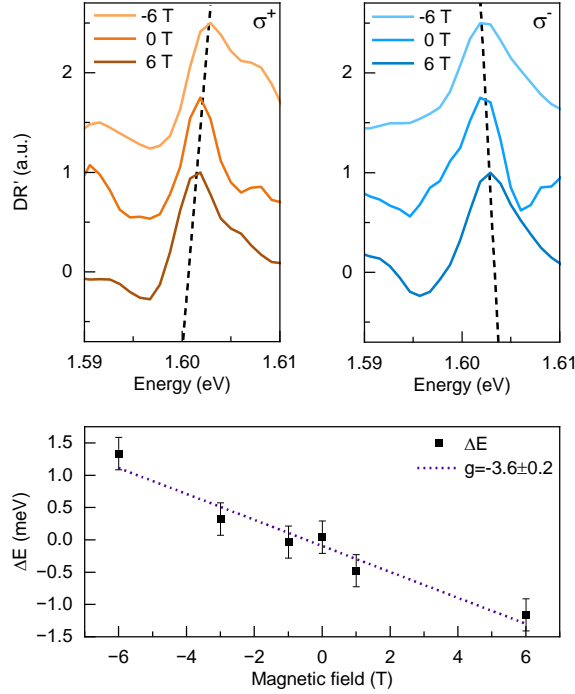


FIG. S4. Measurement procedure of the exciton g -factors. Top panel: representative spectra of the narrow-band modulation signal as obtained in circular polarization (σ^+ and σ^-) for linearly polarized excitation at magnetic fields between $B = -6$ T and $B = 6$ T. For each data point, the peak energy was obtained from the maximum of the signal, where an uncertainty of 10% of the linewidth was assumed. Bottom panel: the valley Zeeman splitting between the peak energies in the two polarization branches determines ΔE . The g -factor was obtained from the linear slope of the fit of ΔE as a function of B .

To calculate the g -factors of moiré excitons one needs to determine the g -factor dependence on the wave vector in the corresponding monolayers. For large momentum mismatch $\Delta \mathbf{K}$, this dependence cannot be simply approximated by a paraboloid at the \mathbf{K} or \mathbf{K}' points. Thus, the g -factor of the moiré exciton m is written as

$$g_m = \sum_l \sum_{\mathbf{K}} \sum_{\mathbf{k}} c_{l,m}(\mathbf{K}) \phi_{\mathbf{k}} [g_{l,e}(\mathbf{k}, \mathbf{K}) + g_{l,h}(\mathbf{k}, \mathbf{K})], \quad (2)$$

where we sum over the two layers $l = 1, 2$ and the vectors of COM and relative motion \mathbf{K} and \mathbf{k} . Here, $\phi_{\mathbf{k}}$ is the relative wavefunction, $c_{l,m}(\mathbf{K})$ are coefficients related to the plane-wave projections $\langle j(l, \mathbf{K}) | m \rangle$, and $g_{l,e}(\mathbf{k}, \mathbf{K})$ and $g_{l,h}(\mathbf{k}, \mathbf{K})$ are g -factors of the electron and hole.

REAL SPACE DISTRIBUTION OF MOIRÉ EXCITON STATES

To compute the real-space distribution of the emerging moiré excitons we denote the original basis of the Hamiltonian (1) in the main text by $|j\rangle$ with $j = 0, \dots, 12$, s.t. it holds e.g. $\langle j|H|j\rangle = E_j$ for $j = 0, \dots, 6$ and $\langle j|H|j\rangle = E_{j-7}$ for $j = 7, \dots, 12$. Similarly, the Hamiltonian's eigenbasis corresponding to the moiré excitons is denoted by $|m\rangle$.

We define $\mathbf{b}_0 = \mathbf{0}$ such that the intralayer states $|j\rangle$, $j = 0, \dots, 6$ correspond to the plane waves $\exp(i\mathbf{b}_j\mathbf{r})$. Then, the intralayer distribution of the moiré excitons $|m\rangle$ is simply computed by the plane-wave projections of these first seven states, *i.e.*, $\psi_m(\mathbf{r}) = \sum_{j=0}^6 \langle j|m\rangle e^{i\mathbf{b}_j\mathbf{r}}$. Using this formula for the bright moiré excitons results in the plots in Fig. 4 of the main text.

Similarly, the interlayer distribution is obtained from projections on the six interlayer states, $\tilde{\psi}_m(\mathbf{r}) = \sum_{j=7}^{12} \langle j|m\rangle e^{i\mathbf{b}_j\mathbf{r}}$, where we define \mathbf{b}_j as the vectors pointing to the blue states defined in Fig. 1 of the manuscript (cp. Eq. 2 of the main text). Interestingly, comparing the intra- and interlayer distributions helps to provide an intuition on the coupling strengths between intra- and interlayer excitons which we specify for the peaks $M_2(-10\text{V})$ and M_3 in Fig. S5. If we plot the overlap of the respective wave functions for each branch as shown in the bottom panel, one easily sees that the overlap for the M_3 doublet is much larger than for the M_2 peak, resulting in the strongest anti-crossing as observed in Fig. 3 of the main text.

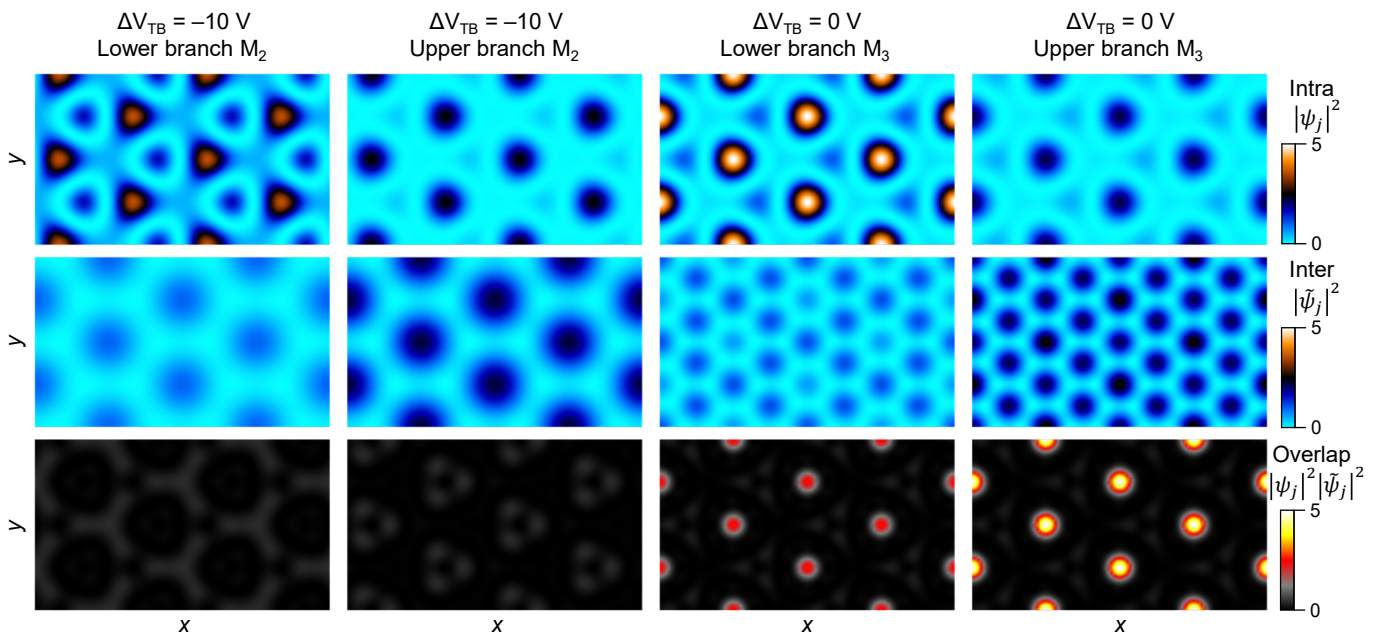


FIG. S5. The upper and middle panels show spatial distributions of intra- and interlayer exciton wave functions of the peaks $M_2(-10\text{V})$ and M_3 , respectively. The bottom panel shows their wave functions overlap with the strongest overlap for the M_3 doublet.

LIMITING CASES OF THE EFFECTIVE MODEL

The phenomenological model developed in the main text presents a combination of intralayer exciton mixing mediated by the potential V and interlayer hybridization mediated by the hopping parameter t . Conversely, setting $V = 0$ meV recovers the pure interlayer hybridization model, and setting $t = 0$ meV results in a pure intralayer exciton mixing description.

To assess these two descriptions, we fabricated a second sample in R-type stacking configuration. In Fig. S6a, we show the experimental DR signals of both samples together with theoretical fits in both limiting cases of the model. The good agreement between theory and experiment shows that both the $V = 0$ meV and $t = 0$ meV subspaces provide enough descriptive power to model the neutral spectra of both H- and R-type devices. Therefore, further experimental data is needed in order to determine the correct contributions to the intra- and interlayer moiré potentials.

Notably, in the $V = 0$ meV description, any exciton mixing is mediated through second-order hopping processes and is associated with substantial out-of-plane electric dipoles as shown in Fig. S6b. To describe the vanishing electric-field dispersion of the bright excitons as observed in experiment, it is therefore necessary to include the potential V to enable first-order intralayer coupling. The strong avoided crossing of M_3 in the H-type data, on the contrary, requires finite interlayer hybridization. Therefore, to correctly describe all three bright excitons, it is necessary to combine both intralayer coupling and interlayer hybridization as shown in Fig. 2b of the main text.

Finally, to illustrate the quantitative impact of the most important fitting parameters, we show the evolution of the computed absorption spectra with the varying parameters θ , $|V|$, $arg(V)$ and t in Fig. S7.

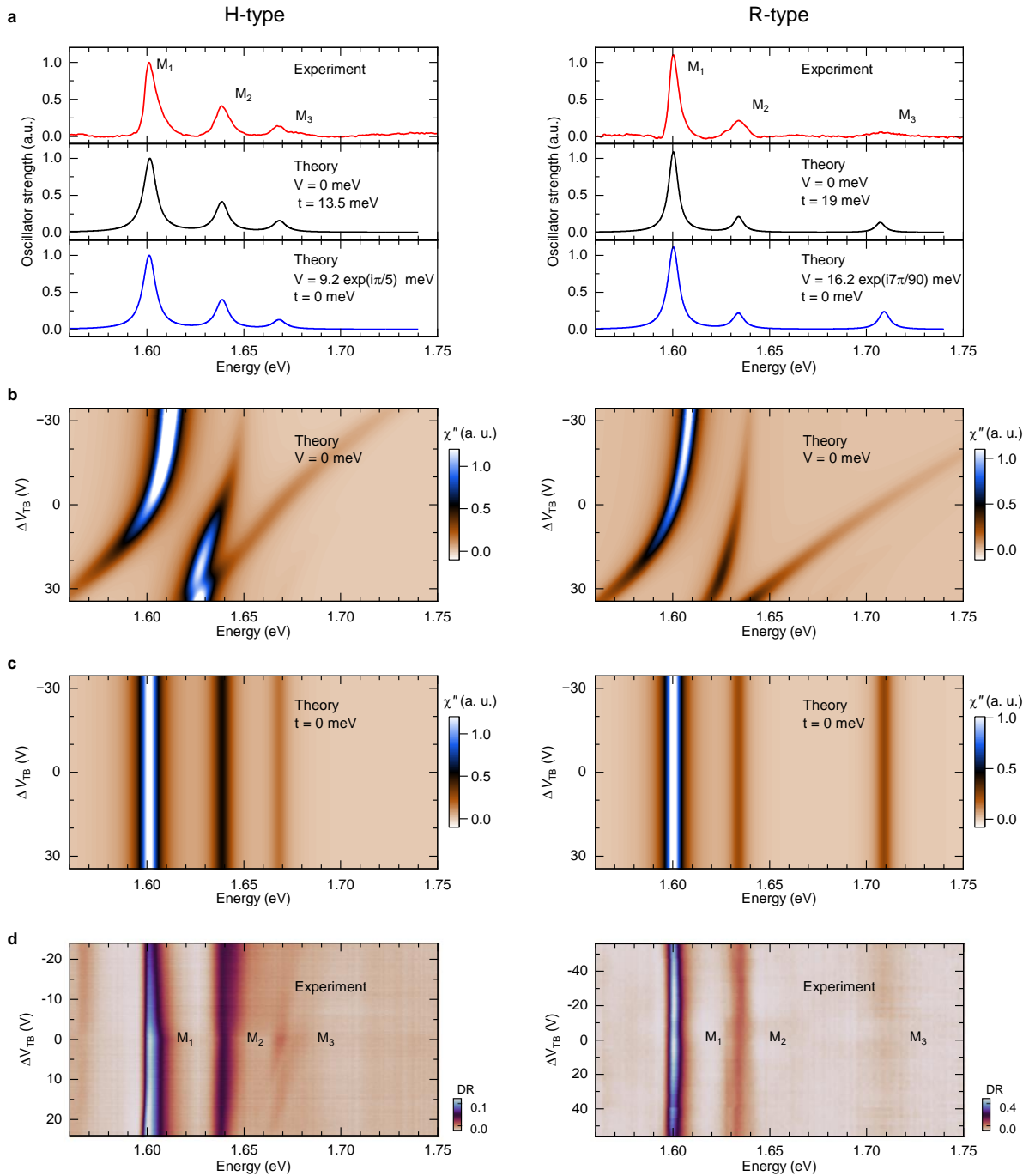


FIG. S6. Comparison of experimental data and modeling by the limiting cases $V = 0$ meV and $t = 0$ meV, only. The left column refers to H-type data as shown in the main text, and the right column to R-type data. **a.** Experimental DR spectra with the three bright moiré excitons (note that in the R-stacking, M_3 appears 45 meV blue-shifted with respect to M_3 in the H-stacking, which is a consequence of the reversed ordering of the spin-polarized conduction sub-bands), complemented with theoretical fits of the neutral spectra within the interlayer hybridization model ($V = 0$ meV) or within the intralayer mixing model ($t = 0$ meV) only. For the neutral regime, very good agreement between experiment and both theories can be obtained. **b & c.** Calculated dispersions under perpendicularly applied electric fields for $V = 0$ meV (**b**) and $t = 0$ meV (**c**). **d.** Actual experimental dispersions of the three bright moiré excitons. In particular, there is no sizable energetic shifts for M_1 and M_2 in both stacking configurations, contrary to what the hybridization model predicts. However, M_3 presents an avoided crossing with a sizable Stark shift in the H-type data, contrary to the $t = 0$ meV simulation.

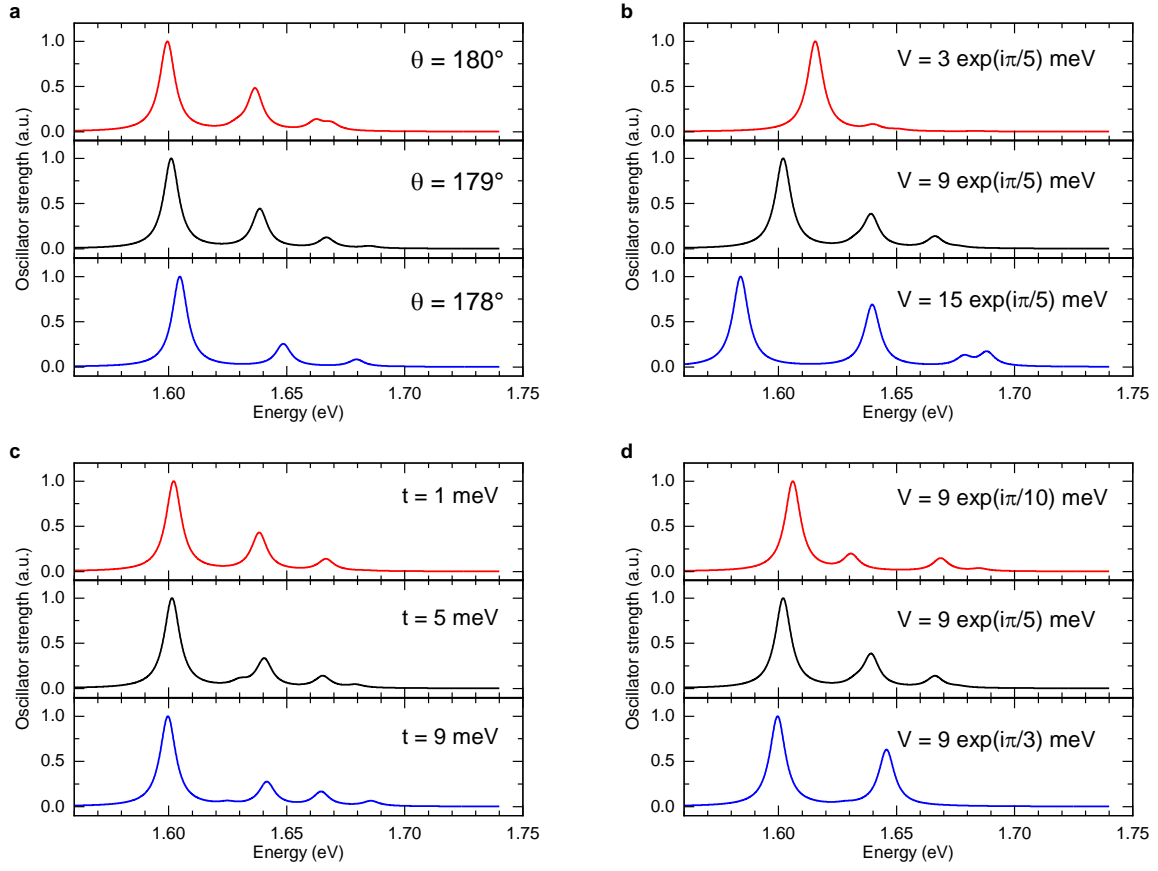


FIG. S7. Evolution of the computed spectra when all parameters but one are kept constant, with varying θ in (a), $|V|$ in (b), t in (c) and $\arg(V)$ in (d).

-
- [1] A. Arora, A. Mandal, S. Chakrabarti, and S. Ghosh, Magneto-optical Kerr effect spectroscopy based study of Landé g-factor for holes in GaAs/AlGaAs single quantum wells under low magnetic fields, *J. Appl. Phys.* **113**, 213505 (2013).
 - [2] S. Zhao, Z. Li, X. Huang, A. Rupp, J. Göser, I. A. Vovk, S. Yu. Kruchinin, K. Watanabe, T. Taniguchi, I. Bilgin, A. S. Baimuratov, and A. Högele, Excitons in mesoscopically reconstructed moiré heterostructures, *Nat. Nanotechnol.* **18**, 572 (2023).
 - [3] J. D. E. McIntyre and D. E. Aspnes, Differential reflection spectroscopy of very thin surface films, *Surf. Sci.* **24**, 417 (1971).
 - [4] B. Alén, F. Bickel, K. Karrai, R. J. Warburton, and P. M. Petroff, Stark-shift modulation absorption spectroscopy of single quantum dots, *Appl. Phys. Lett.* **83**, 2235 (2003).